Supporting Information for:

Highly Sensitive Wireless Dual-Spiral Resonant Contact Lens for Continuous Intraocular Pressure Monitoring

Ying Liu[a], Zhixian Chen[a], Xiaoyu Zhao[a], Lin Xu[b] and Shengli Mi[a*]

[a]Bio-manufacturing Engineering Laboratory, Tsinghua Shenzhen International Graduate School, Tsinghua University, Shenzhen, Guangdong, 518000, China.

[b]Shenzhen Eye Hospital, 18 Fengtian Road, Shenzhen, Guangdong, 518040, China.

***Corresponding author:**

Shengli Mi

Tsinghua Shenzhen International Graduate School, Tsinghua University,

Rm 1110, Energy and environment Building, Tsinghua Campus,

The University Town, Shenzhen 518055, P. R. China

Tel: +86 (0)755 26036329;

Fax: +86(0)755 26036356;

E-mail: mi.shengli@sz.tsinghua.edu.cn

Supplementary Note 1: Analysis of Signal Quality Factor

This note provides the detailed data supporting the analysis of signal quality factors (Q-factor) discussed in Sections 2.3 and 2.4 of the main text. The Q-factor and resonance depth (S_{11} magnitude at f_0) were calculated from the original S_{11} spectral data used to generate Fig. 4c (biomimetic eye) and Fig. 5c (porcine eye).

The -3 dB bandwidth (Δf) was determined from the S_{11} parameter spectra by finding the frequency width at which the magnitude increased by 3 dB from the resonance dip minimum. The Q-factor was then calculated using the formula:

$$Q = \frac{f_0}{\Delta f}$$

where f_0 is the resonant frequency at the dip minimum.

Table S1. Signal quality analysis for the D1–AN sensor on the biomimetic eyeball platform (data source: Fig. 4c).

IOP (mmHg)	Resonant Frequency, f_0 (MHz)	Resonance Depth (dB)	-3 dB Bandwidth, Δf (MHz)	Q-Factor
5	824.6856	-9.9058	17.2222	47.8865
10	811.2624	-10.688	15.7824	51.4039
15	801.4347	-11.6429	14.9863	53.4778
20	790.6482	-12.0628	16.0215	49.3498
25	781.0602	-12.4984	15.5054	50.374
30	773.8692	-12.8952	14.9858	51.6436
35	766.6782	-14.1615	13.6002	56.3728
40	757.3299	-14.4731	13.2493	57.1592
45	747.9816	-15.0341	12.3354	60.6351
50	738.873	-16.0691	11.624	63.565

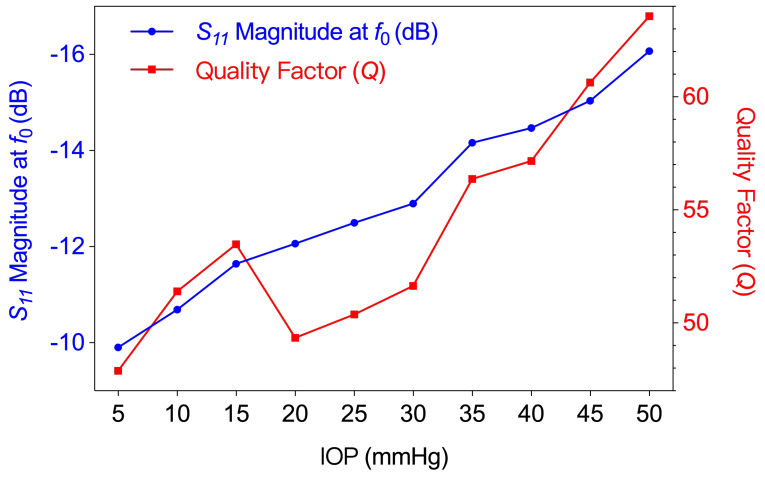

Supplementary Fig. S1. Dependence of the Q-factor and the resonance depth (S_{11} magnitude at f_0) on the applied intraocular pressure (IOP) for the biomimetic eyeball platform. The solid lines guide the eye to illustrate the increasing trend of Q-factor.

Table S2. Signal quality analysis for the D1–AN sensor on ex vivo porcine eyes (data source: Fig. 5c).

IOP (mmHg)	Resonant Frequency, f_0 (MHz)	Resonance Depth (dB)	-3 dB Bandwidth, Δf (MHz)	Q-Factor
30	780.31	-10.425	7.65	101.95
25	783.21	-10.154	7.67	102.07
20	786.21	-9.662	7.98	98.50
15	789.01	-9.293	8.20	96.22
10	792.41	-8.927	8.56	92.60
5	795.61	-8.616	8.89	89.51

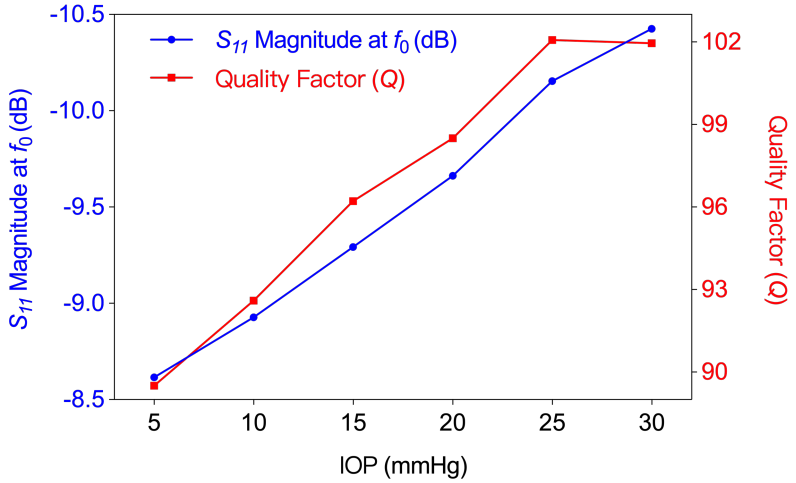

Supplementary Fig. S2. Dependence of the Q-factor and the resonance depth (S_{11} magnitude at f_0) on the applied IOP for ex vivo porcine eyes. The solid lines guide the eye to illustrate the overall trend of Q-factor variation in biological tissue.

Supplementary Note 2: Experimental Validation of the Equivalent Circuit Model

The dual-layer spiral structure of the contact lens sensor acts as a distributed resonator where the two spiral layers are electrically connected as a whole. While the absolute capacitance of such a distributed system with fringing fields cannot be accurately calculated using a simple parallel-plate formula—requiring full-wave 3D electromagnetic simulations (e.g., HFSS or CST) for precise quantification—the macroscopic capacitance change can still be effectively expressed by this model. Because our optimal design (D1–AN) utilizes an axisymmetric anti-parallel configuration, the electric field is expected to be predominantly confined within the intermediate PDMS dielectric layer (as illustrated in Fig. 2c). This confinement enables the device to macroscopically behave in a manner that is highly consistent with a parallel-plate capacitor (Eq. 1) under mechanical deformation.

To experimentally substantiate the validity of this equivalent circuit model and the associated formulas (Eqs. 1–3 in the main text), we further analyzed the relationship between the resonant frequency (f_0) and the applied IOP. The resonant frequencies were extracted from the original S_{11} spectra measured on the biomimetic eyeball (Fig. 4c) and ex vivo porcine eyes (Fig. 5c). According to the resonant frequency equation ($f_0 = 1/2\pi\sqrt{LC}$), the term $1/f_0^2$ is directly proportional to the product of the effective inductance and capacitance ($L \cdot C$). As shown in Figs. S3 and S4, $1/f_0^2$ demonstrates a highly linear relationship with the applied IOP on both the biomimetic eyeball platform (R^2=0.9977) and ex vivo porcine eyes (R^2=0.9994), respectively. This macroscopic linearity strongly supports the use of the proposed equivalent circuit framework and indicates that the IOP-induced variation in the effective resonant parameters can be effectively described at the device level by the theoretical formulas.

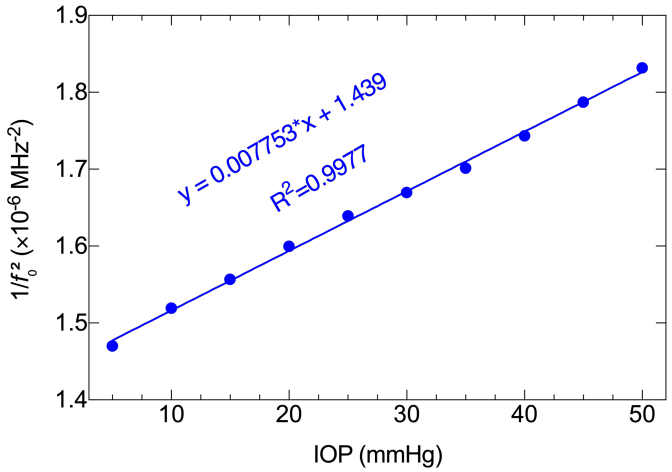

Supplementary Fig. S3. Linear relationship between $1/f_0^2$ and the applied IOP on the biomimetic eyeball platform (data derived from Fig. 4c). The high macroscopic linearity supports the use of the equivalent circuit model and the parallel-plate capacitance formula at the device level.

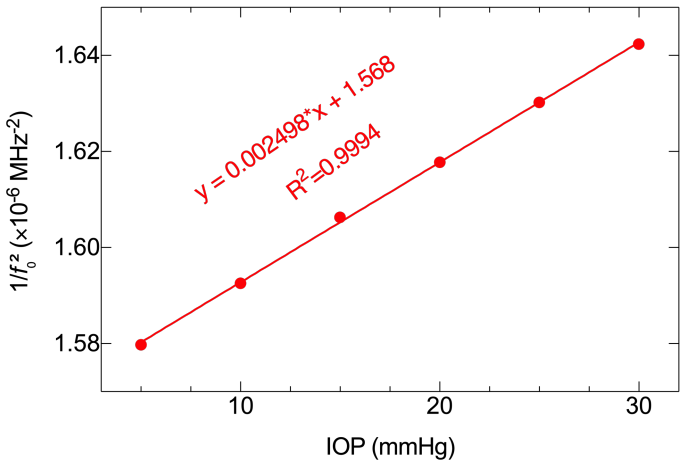

Supplementary Fig. S4. Linear relationship between $1/f_0^2$ and the applied IOP on ex vivo porcine eyes (data derived from Fig. 5c). The high macroscopic linearity supports the use of the equivalent circuit model and the parallel-plate capacitance formula at the device level.

Supplementary Note 3: Effect of Readout Distance and Angular Misalignment on Sensor Performance

To rigorously assess the robustness of the wireless contact lens (WCL) sensor against realistic misalignment induced by natural eye movements, we systematically evaluated the impact of readout distance and angular tilt on the sensor's electromagnetic response. The experiments were conducted on the biomimetic eyeball platform under a constant IOP.

First, the vertical separation distance between the reader coil and the sensor was varied from 4 mm to 12 mm in 1 mm increments (Fig. S5). As expected, increasing the distance reduces the mutual inductance between the coils, leading to a gradual attenuation of the S_{11} resonance dip depth (amplitude). Crucially, the resonant frequency—the core parameter encoding the IOP variations—remained exceptionally stable, exhibiting a maximum shift of less than 0.15 MHz across the entire tested distance range.

Second, the angular misalignment was evaluated by tilting the reader coil relative to the sensor plane from 0° to 45° in 15° increments, maintaining a nominal standoff distance (origin-to-origin) of 6 mm (Fig. S6). Similar to the distance variation, the angular tilt caused a progressive decrease in the resonance amplitude due to the reduced magnetic flux linkage. However, the induced resonant frequency drift was completely negligible (< 0.15 MHz).

In all tested configurations, the resonance peak remained clearly distinguishable, allowing for reliable signal extraction. These results collectively demonstrate that while structural misalignment affects the signal coupling strength, the frequency-encoded

IOP reading is inherently robust to moderate spatial and angular variations. These results support the feasibility of the proposed WCL device for reliable, continuous IOP monitoring under moderate readout misalignment conditions relevant to natural ocular dynamics.

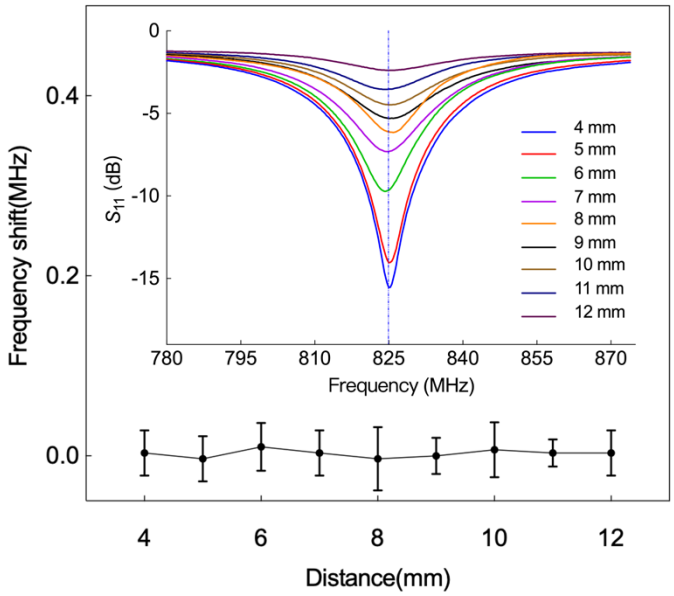

Supplementary Fig. S5. Effect of readout distance on the sensor response. S_{11} spectra (inset) and the corresponding resonant frequency shift as a function of the vertical distance (4 to 12 mm) between the reader coil and the contact lens sensor. The resonant frequency exhibits high stability (maximum frequency shift < 0.15 MHz) despite the attenuation in signal amplitude, confirming the robustness of the frequency-based sensing mechanism. Data are presented as mean ± SD (n = 3).

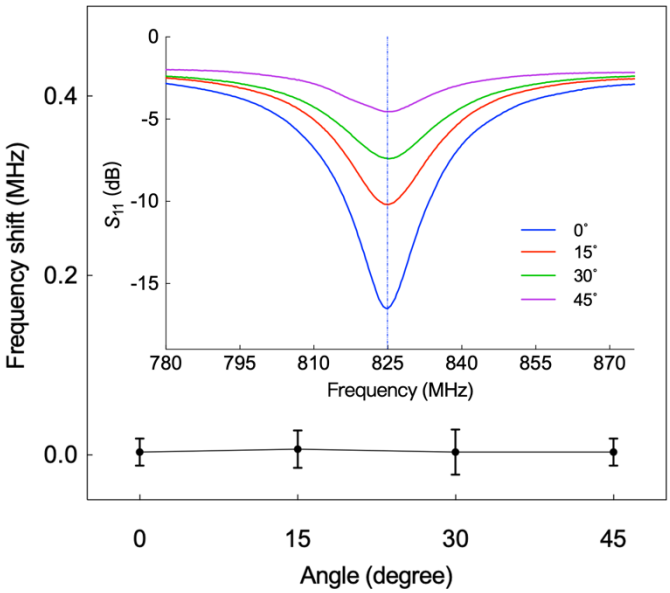

Supplementary Fig. S6. Effect of angular misalignment on the sensor response. S_{11} spectra (inset) and the corresponding resonant frequency shift under varying angular misalignments (0° to 45°) at a fixed readout distance of 6 mm. The resonant frequency remains highly stable (maximum frequency shift < 0.15 MHz) even as the signal amplitude decreases with tilt, further validating the reliability of the readout protocol. Data are presented as mean ± SD (n = 3).

Supplementary Note 4: Thickness Specifications of the Functional Circuit Layers

To quantitatively determine the structural dimensions of the sensor—parameters that critically influence both mechanical compliance and electromagnetic sensitivity—cross-sectional characterization was performed using field-emission scanning electron microscopy (FE-SEM; SU8010, Hitachi) at an accelerating voltage of 3.0 kV.

To enhance device flexibility and sensitivity, the bulk polyimide (PI) substrate was selectively removed during fabrication via alkaline wet etching (1 mol/L KOH solution at 70 °C for 20 min). After etching, the PI substrate was completely removed, leaving only the thermoplastic polyimide (TPI) bonding layer (2 μm) as the remaining flexible support.

As shown in Supplementary Fig. S7, the cross-sectional SEM image reveals a thin and well-defined multilayer structure. The base layer consists of a 2 μm TPI bonding layer, originally used for thermal lamination of the Cu foil and resistant to KOH etching. The primary conductive layer is an electroplated copper (Cu) layer with a thickness of 18 μm, which minimizes high-frequency resistive loss while maintaining mechanical flexibility. On top of the Cu layer, a 2 μm nickel (Ni) barrier layer is deposited, followed by a thin gold (Au) surface coating (~0.1 μm) to enhance chemical stability and biocompatibility. Due to its small thickness, the Au layer is not clearly resolved in the SEM image, and its thickness is primarily determined from deposition parameters.

Thickness values were estimated from SEM cross-sectional images using the scale bar and averaged over multiple regions. Minor interfacial roughness observed between layers arises from electroplating morphology and does not affect electrical continuity or device performance.

The resulting total thickness of the functional stack is 22.1 μm. This thin configuration enables the device to conform closely to the corneal curvature while maintaining structural integrity, and contributes to the high sensitivity of the sensor by facilitating efficient transduction of IOP-induced mechanical deformation into measurable electrical responses.

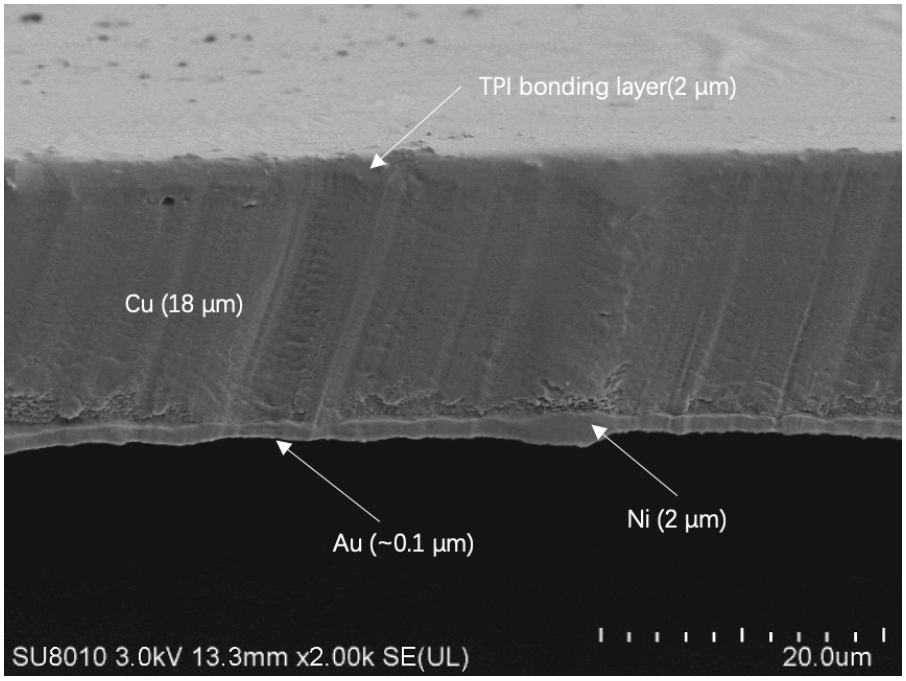

Supplementary Fig. S7. Cross-sectional FE-SEM image of the functional circuit layers after alkaline wet etching of the bulk PI substrate. The remaining structure consists of a 2 μm TPI bonding layer, a ~18 μm electroplated copper (Cu) layer, a 2 μm nickel (Ni) barrier layer, and a thin gold (Au) coating (~0.1 μm). The Au layer is not clearly resolved due to its small thickness. These well-defined and thin multilayer structures are essential for achieving both high mechanical compliance and enhanced electromagnetic sensitivity.

Supplementary Note 5: Fabrication Reproducibility and Practical Tolerance to Folding-Induced Misalignment

To evaluate the reproducibility of the manual folding process and to indirectly assess the practical influence of folding-induced misalignment on device performance, we measured the baseline resonant frequencies (f_0) of multiple independently fabricated sensor prototypes.

As shown in the device architecture in Fig. 1 of the main text, the upper and lower spiral circuits are patterned on a single continuous flexible substrate and remain connected by a central bridge prior to folding. During the folding process, this bridge acts as a self-constraining structural hinge, which limits large translational and rotational displacement between the two spiral layers. In addition, the optimized D1–AN design adopts a gradient line-width strategy, in which the outermost traces are widened to 0.50 mm. This structural feature improves tolerance to small folding-induced local offset and helps maintain effective overlap between the two folded spiral layers.

From a first-order theoretical perspective, substantial lateral misalignment would reduce the effective overlap area between the two spiral layers, thereby decreasing the effective interlayer capacitance. According to the resonant relation $f_0 = 1/(2\pi\sqrt{LC})$, such a capacitance reduction would shift the baseline resonant frequency upward. In addition, weaker electric-field confinement could slightly reduce the resonance depth and Q-factor, thereby attenuating the apparent signal amplification. Therefore, interlayer misalignment is relevant in principle.

To examine whether such effects are practically significant under the present fabrication process, the baseline resonant frequencies of five independently fabricated

D1–AN sensors were measured under the same biomimetic eyeball condition at 5 mmHg. As summarized in Supplementary Table S3, the measured baseline frequencies showed a narrow distribution, with an average value of 824.82 MHz and a standard deviation of 0.81 MHz. The narrow device-to-device variation in baseline resonant frequency (824.82 ± 0.81 MHz, n = 5) provides practical, though indirect, evidence that any residual folding-induced misalignment is not large enough to cause a substantial change in the baseline electromagnetic response of the device. These results support the conclusion that the combined structural constraint of the central bridge and the widened outer traces provides sufficient practical tolerance for reproducible device fabrication.

Table S3. Baseline resonant frequencies of five independently fabricated D1–AN contact lens sensors measured under the same biomimetic eyeball condition at 5 mmHg.

Sensor Prototype	**Baseline Resonant Frequency, f_0 (MHz)**
Sample 1	824.68
Sample 2	825.12
Sample 3	823.95
Sample 4	826.04
Sample 5	824.31
Mean ± SD	824.82 ± 0.81

Supplementary Note 6: Cost Estimation and Manufacturing Scalability

To evaluate the potential for large-scale commercialization, a preliminary cost estimation was conducted based on the current batch-fabrication process. The dual-spiral sensing circuit was fabricated using standard flexible printed circuit (FPC) technology. A commercial FPC panel (240 mm × 240 mm), costing approximately 800 RMB (~110 USD), can accommodate 144 sensor units, corresponding to a per-unit circuit cost of approximately 5.6 RMB (~0.77 USD). In addition, the encapsulation requires ~1 g of PDMS per device, contributing approximately 0.72 RMB (~0.10 USD) to the material cost. Thus, the total direct material and panel-level fabrication cost of the sensor unit is estimated to be below 7 RMB (<1 USD) per device.

This estimate reflects the direct cost of the sensor unit at the prototype batch level and does not include labor, packaging, sterilization, quality control, reader integration, or regulatory costs. From a manufacturing perspective, the optimized D1–AN design employs gradient line widths ranging from 0.50 mm to 0.125 mm, which are fully within the processing capability of standard commercial FPC foundries. Therefore, the device can be fabricated using mature panel-level FPC manufacturing routes without relying on wafer-level processing or semiconductor-grade cleanroom conditions.

In addition to its low direct cost, the proposed device retains several features favorable for future translation, including passive wireless operation, the absence of rigid integrated circuits or on-board power components, and compatibility with panel-level batch fabrication. Further cost reduction may be achieved through automated folding/alignment, batch PDMS encapsulation, and yield optimization in industrial

production. Overall, these results support the potential of the proposed device for scalable and cost-effective future commercialization.

Supplementary Note 7: Geometric Characterization and Ergonomic Considerations of the Smart Contact Lens

The geometric profile of a contact lens, including its thickness distribution, diameter, and base curve, is an important factor affecting wearing comfort and physiological compatibility. To evaluate the structural feasibility of the proposed smart contact lens, the geometric parameters of the fully fabricated device were characterized.

The integrated smart contact lens has an overall diameter of 14.2 mm and a base curve of 8.6 mm, both of which fall within the typical range of soft contact lenses. Cross-sectional optical microscopy revealed a region-dependent thickness distribution. The central optical zone, which is free of the resonator structure, had a thickness of approximately 130 ± 8 μm. In the mid-peripheral functional region containing the embedded resonator, the total local thickness of the integrated lens was approximately 200 ± 10 μm. Within this region, the embedded single resonator stack accounts for approximately 69 μm of the thickness, as estimated from the layer thicknesses determined by cross-sectional SEM analysis in Supplementary Note 4 (~22.1 μm for each functional circuit layer) together with the nominal PDMS dielectric thickness (~25 μm).

Compared with conventional vision-correction soft contact lenses, the functional region of the present device is thicker. However, the central optical zone remains relatively thin, which is beneficial for minimizing interference with the visual axis. In addition, the maximum local thickness of the present device (200 μm) remains substantially lower than that reported for previously described smart contact lens systems such as the Sensimed Triggerfish® (585 μm). The overall diameter and base curve of the present

lens are also comparable to those of commercially available soft contact lenses.

The overall thickness distribution and curved lens geometry are expected to help mitigate eyelid interaction during blinking. Moreover, the lens matrix is primarily composed of PDMS, a material with high intrinsic oxygen permeability, which is expected to partially mitigate the physiological burden associated with increased local thickness. Although a full device-level oxygen transmissibility evaluation and direct wear-comfort assessment were not performed in the present study, the geometric and material characteristics of the device support the preliminary thickness feasibility of the proposed design and suggest potential ergonomic compatibility for future wearable ophthalmic applications.

Table S4. Comparison of geometric parameters of the proposed device and representative contact lens systems.

Category	**Material**	**Maximum thickness (μm)**	**Diameter (mm)**	**Base curve (mm)**	**Oxygen permeability (barrers)**	**Functional integration**
Commercial contact lenses	Hydrogel / Silicone hydrogel	70–100	14.0–14.2	8.4–8.8	25–100	Vision correction only
Scleral lenses	RGP materials	150–400	14.5–18.0	Variable	50–100	Corneal protection / therapeutic use
Sensimed Triggerfish ®	Medical silicone	585	14.1	8.4 / 8.7 / 9.0	~350	IOP sensing
Recent literature reports	Various materials	150–500	14.0–14.5	8.4–9.0	Various	Sensing functions
This work	PDMS	200	14.2	8.6	600–800	IOP sensing

Note: The geometric and oxygen-permeability values for commercial soft contact lenses, scleral lenses, Sensimed Triggerfish®, and representative literature reports are literature-based estimates intended for qualitative comparison. The oxygen permeability value reported for this work (600–800 barrers) refers to the intrinsic material-level permeability of PDMS rather than the oxygen transmissibility (Dk/t) of the fully integrated device.

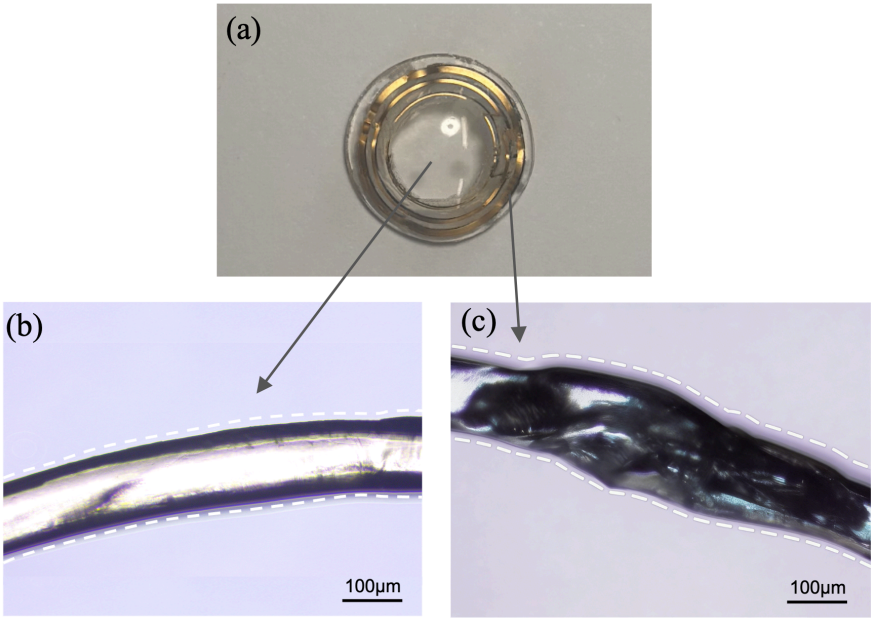

Supplementary Fig. S8. Geometric characterization of the smart contact lens. (a) Photograph of the fabricated smart contact lens. (b) Cross-sectional optical microscopy image of the central optical zone, showing a thickness of approximately 130 ± 8 μm. (c) Cross-sectional optical microscopy image of the mid-peripheral functional region containing the embedded resonator, showing a total local thickness of approximately 200 ± 10 μm. Scale bars: 100 μm.

Supplementary Note 8: Analysis of Detection Sensitivity and Reliability in Clinically Critical IOP Ranges

To comprehensively evaluate the clinical relevance of the proposed WCL sensor, we analyzed its detection sensitivity and signal reliability across three clinically relevant IOP ranges.

In the present study, the IOP response was analyzed according to three clinically relevant zones[8,12]:

- Hypotony Range (<10 mmHg): Associated with postoperative complications (e.g., hypotony syndrome) or uveitis. Accurate identification of this low-pressure state is important for preventing ocular hypotony-related complications.
- Normal Range (10–21 mmHg): The physiological range for healthy individuals and a clinically important interval for detecting subtle fluctuations, particularly in normal-tension glaucoma patients.
- Glaucoma / High-Risk Range (>21 mmHg): Covers pathologically elevated IOP conditions relevant to glaucoma diagnosis and management, including both chronic ocular hypertension and acute pressure spikes.

1. Segmented Detection Sensitivity Across Clinical Ranges

To visually correlate the sensor's response with clinical benchmarks, the calibration curves have been replotted with background shading to demarcate the Hypotony, Normal, and Glaucoma ranges. We performed segmented linear regression analysis to quantitatively assess performance within these specific states.

On the highly controlled biomimetic eyeball platform, the sensors exhibited reliable linear responses across the entire tested spectrum (5–50 mmHg), as summarized in Table S5. The segmented calibration curves for the axisymmetric designs (D1–D3) and the point-symmetric design (D4) are presented in Figs. S9 and S10, respectively.

Table S5. Segmented sensitivity and linearity of sensors on the biomimetic platform across different clinically relevant IOP ranges.

Sensor	IOP Range (mmHg)	Physiological State	Data Points Used	Sensitivity (MHz/mmHg)	Linearity (R^2)
D1–AN	< 10	Hypotony Range	5, 10	-2.687	N/A*
	10 – 21	Normal Range	10, 15, 20	-2.047	0.9993
	> 21	Glaucoma Range	20 to 50	-1.704	0.9988
D2–AU	< 10	Hypotony Range	5, 10	-1.247	N/A*
	10 – 21	Normal Range	10, 15, 20	-0.768	0.9252
	> 21	Glaucoma Range	20 to 50	-0.945	0.9925
D3–AW	< 10	Hypotony Range	5, 10	-0.467	N/A*
	10 – 21	Normal Range	10, 15, 20	-0.390	0.9692
	> 21	Glaucoma Range	20 to 50	-0.395	0.9869
D4–PN	< 10	Hypotony Range	5, 10	-0.367	N/A*
	10 – 21	Normal Range	10, 15, 20	-0.233	0.9347
	> 21	Glaucoma Range	20 to 50	-0.248	0.9889

Note: In the hypotony range (<10 mmHg), the linearity correlation coefficient (R^2) is marked as N/A because only two empirical data points (5 and 10 mmHg) fall strictly within this interval, making a linear fit statistically trivial. The sensitivity value reported represents the direct slope between these two points.

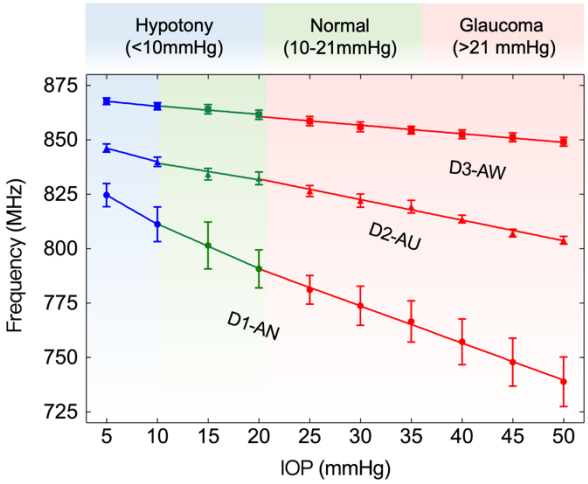

Supplementary Fig. S9. Segmented calibration curves for axisymmetric designs (D1–D3) on the biomimetic eyeball platform. The background shading explicitly demarcates the Hypotony (<10 mmHg, gray), Normal (10–21 mmHg, green), and Glaucoma (>21 mmHg, red) ranges. Dotted lines represent the segmented linear regression for each clinical interval.

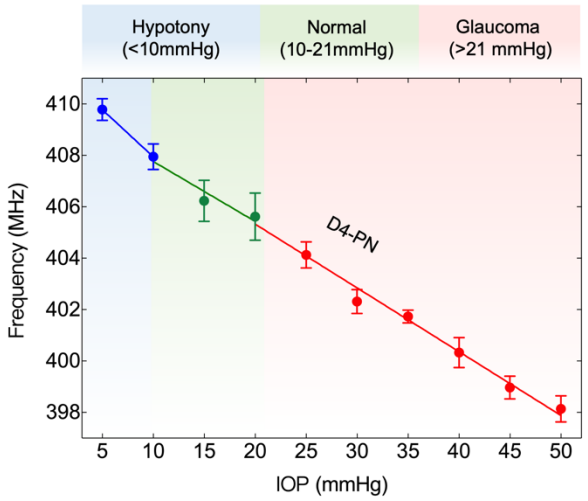

Supplementary Fig. S10. Segmented calibration curve for the point-symmetric design (D4–PN) on the biomimetic eyeball platform. Similar to the axisymmetric

designs, the D4–PN sensor maintains linear trackability across all three clinically relevant zones, though with relatively lower sensitivity compared to D1–AN.

To further validate the sensor's capability on biologically complex tissues, we evaluated its segmented sensitivity on *ex vivo* porcine eyes (Table S6 and Fig. S11). In the critical Normal Range (10–21 mmHg), the three samples exhibited striking consistency, yielding sensitivities of -0.760, -0.770, and -0.760 MHz/mmHg, with excellent linearity ($R^2 \geq 0.9932$).

This pronounced attenuation in sensitivity at elevated pressures (>21 mmHg) observed in biological tissue is fundamentally driven by the inherent biomechanical properties of the cornea. Unlike the synthetic elastomer used in our biomimetic platform (which exhibits a relatively gradual stiffening), the biological cornea possesses a complex collagen fibril network that demonstrates a highly nonlinear, "J-shaped" stress-strain response. At lower pressures, the tissue is highly compliant, resulting in maximal mechanical deformation and thus the highest sensitivity. As IOP increases into the pathological glaucoma range, these collagen fibers recruit and become taut, causing the corneal tissue to stiffen exponentially. Remarkably, the D1–AN sensor maintains continuous and approximately linear ex vivo trackability of IOP variations even at these higher pressures.

Table S6. Segmented sensitivity and linearity of the D1–AN sensor on ex vivo porcine eyes (n = 3) across clinically relevant IOP ranges.

Sample	IOP Range (mmHg)	Physiological State	Data Points Used	Sensitivity (MHz/mmHg)	Linearity (R^2)

Eye 1	< 10	Hypotony Range	5, 10	-1.080	N/A*
	10 – 21	Normal Range	10, 15, 20	-0.760	1.0000
	> 21	Glaucoma Range	20, 25, 30	-0.470	0.9751
Eye 2	< 10	Hypotony Range	5, 10	-1.100	N/A*
	10 – 21	Normal Range	10, 15, 20	-0.770	0.9932
	> 21	Glaucoma Range	20, 25, 30	-0.380	0.9918
Eye 3	< 10	Hypotony Range	5, 10	-0.820	N/A*
	10 – 21	Normal Range	10, 15, 20	-0.760	0.9991
	> 21	Glaucoma Range	20, 25, 30	-0.530	0.9989

Note: In the hypotony range (<10 mmHg), the linearity correlation coefficient (R^2) is marked as N/A because only two empirical data points (5 and 10 mmHg) fall strictly within this interval, making a linear fit statistically trivial. The sensitivity value reported represents the direct slope between these two points.

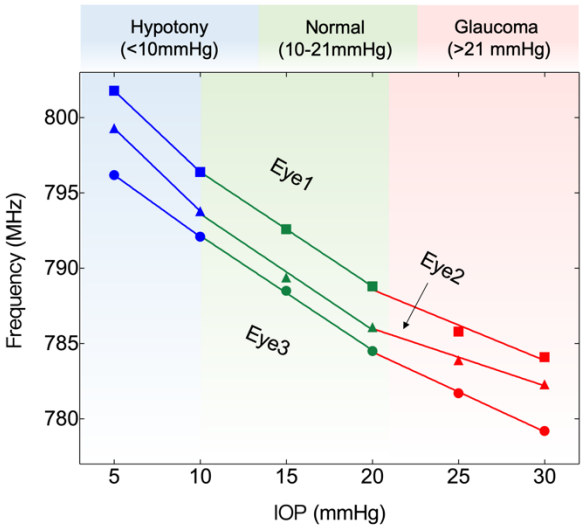

Supplementary Fig. S_{11}. Segmented calibration curves for the D1–AN sensor on ex vivo porcine eyes (n = 3). Each biological sample demonstrates a clear shift in sensitivity as it transitions from the hypotony range into the glaucoma range. This visual

representation underscores the sensor's ability to maintain reliable linear tracking across specimens despite the nonlinear stiffening of biological tissues.

2. Signal Reliability in the Clinically Critical Range

High sensitivity must be accompanied by signal robustness to prevent false readings during continuous monitoring. We utilized the Q-factor and resonance depth (S_{11} magnitude at f_0) to assess signal reliability, specifically focusing on the clinically relevant elevated-IOP range.

Based on the spectral data derived from the *ex vivo* porcine eyes (Table S2), the sensor maintains remarkable signal integrity as the pressure elevates into the pathological zone. Specifically, across the critical 15 to 30 mmHg window, the Q-factor remains stable at an exceptionally high level (96.22 to 101.95). Concurrently, the resonance depth remains strong, deepening from -9.293 dB to -10.425 dB. This consistently high Q-factor (>96) indicates that the resonance dip remains sharp and readily distinguishable from background noise, even when the biological cornea is under elevated stress. Therefore, the sensor exhibits robust detection reliability precisely in the IOP ranges most critical for glaucoma diagnosis and management.

Supplementary Note 9: Extended 5-hour Simulation Test on the Biomimetic Eyeball Platform

To evaluate the temporal stability and long-duration tracking reliability of the WCL sensor, an extended 5-hour simulation test was conducted on the *in vitro* biomimetic eyeball platform. This platform was employed for the long-duration evaluation to avoid the dehydration and biomechanical instability issues commonly associated with prolonged testing on *ex vivo* biological tissues such as porcine eyes.

During the 300-minute test, the IOP was manually adjusted at 20-minute intervals over a dynamic range of 10–45 mmHg. Rather than applying repetitive uniform pressure ramps, a time-varying pressure sequence was designed to represent distinct fluctuation scenarios. This sequence comprised three sub-cycles, each featuring repeated returns to the baseline level of 15 mmHg:

- Cycle 1 (0–100 min, 15→25→10→15 mmHg): Simulated mild daily IOP fluctuations, including a transient physiological pressure dip to 10 mmHg.
- Cycle 2 (100–200 min, 15→35→15 mmHg): Simulated moderate-to-high risk elevations typical in chronic open-angle glaucoma patients.
- Cycle 3 (200–300 min, 15→45→15 mmHg): Simulated an acute extreme pressure spike (e.g., acute angle-closure glaucoma attack) and the subsequent rapid pressure relief.

The time-resolved resonant frequency response (Supplementary Fig. S12) shows that the sensor closely tracked the imposed IOP variations throughout the entire 5-hour test. To assess long-term baseline stability, the resonant responses at 15 mmHg were

compared at the beginning and at the end of each sub-cycle (0, 100, 200, and 300 min). The corresponding resonant frequencies were 801.5, 801.8, 801.4, and 801.6 MHz, respectively, corresponding to a narrow variation range of only 0.4 MHz over the full test duration. This result indicates that no obvious baseline drift occurred during prolonged operation.

In addition to baseline stability, the sensor also exhibited good reproducibility at repeated elevated pressures across different segments. For example, the resonant frequencies recorded at 20 mmHg in four different segments were 790.9, 790.6, 790.7, and 790.7 MHz, respectively. Similarly, the values at 30 mmHg measured in two independent segments were 773.6 and 773.8 MHz. These results collectively confirm the excellent temporal stability, measurement repeatability, and long-duration operational reliability of the proposed WCL sensor, supporting its capability for continuous and sustainable IOP monitoring.

Table S7. Original data of the extended 5-hour continuous simulation test on the in vitro biomimetic eyeball platform.

Cycle	Time (min)	IOP (mmHg)	Resonant Frequency (MHz)
1	0	15	801.50
	20	20	790.90
	40	25	781.20
	60	20	790.60
	80	10	811.25
	100	15	801.80
	120	25	780.80
	140	35	767.10
2	160	25	781.00
	180	20	790.70
	200	15	801.40
3	220	30	773.60

240	45	747.80
260	30	773.80
280	20	790.70
300	15	801.60

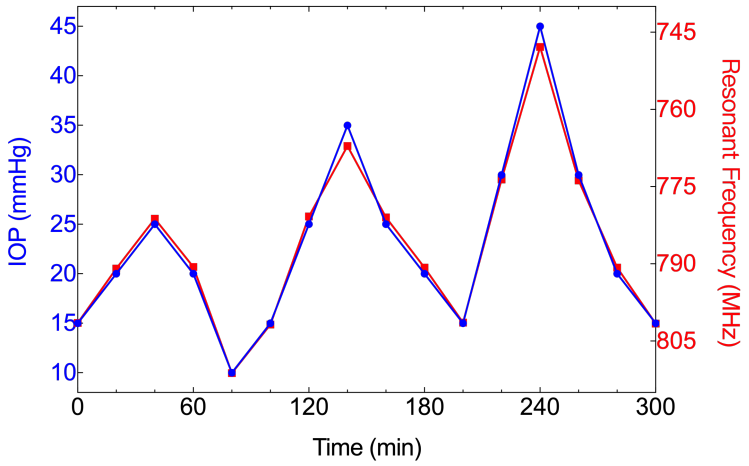

Supplementary Fig. S12. Continuous 5-hour simulation test of the D1–AN sensor on a biomimetic eyeball. Real-time tracking of dynamic IOP variations (10–45 mmHg, blue line) and corresponding resonant frequency (red line) at 20-minute intervals. Across three simulated sub-cycles, the device exhibits highly synchronized tracking, excellent reproducibility at elevated pressures, and no obvious baseline drift upon returning to 15 mmHg (801.4–801.8 MHz), providing strong support for its temporal stability.